ADVANCED MATERIALS INTERFACES
www.advmatinterfaces.de

Spiked Nanostructures Disrupt Fungal Biofilm and Impart Increased Sensitivity to Antifungal Treatment

*Andrew Hayles, Richard Bright, Jonathan Wood, Dennis Palms, Peter Zilm, Toby Brown, Dan Barker, and Krasimir Vasilev**

There is a globally increasing demand for medically implanted devices, partly spurred by an aging population. In parallel, there is a proportionate increase in implant associated infection. Much focus has been directed toward the development of techniques to fabricate nanostructured antimicrobial biomaterials to mitigate infection. The present study investigates the interaction of the fungal pathogen *Candida albicans* with an antimicrobial surface bearing nanoscale protrusions. *C. albicans* cells were observed to be affected by cell wall stress, which impeded its ability to switch to a hyphal phenotype. There are significant differences in the expression of *C. albicans* virulence-associated genes between the untreated and nanostructured surfaces. To determine whether the observed inhibition of *C. albicans* would also sensitize it to antifungal drugs, a culture is established for 3 days on the nanostructured surface before being treated with the antifungal drug amphotericin B. The drug was able to kill all cells on the nanostructured surface at sub-clinical concentrations, while remaining ineffective against cultures grown on a smooth control surface. These findings may eventually prove to be impactful in the clinic, as clinicians may be able to reduce antifungal drug dosages and minimize the effects of drug associated toxicity.

1. Introduction

Titanium-based biomaterials are commonly used as the material of choice for implants for orthopaedics, fracture fixation, and the periodontal field.[1] The superiority of titanium as a biomaterial is reflected in its corrosion resistance, mechanical strength, biocompatibility, and osseointegration capabilities.[1a] Although there is a high success rate associated with implanted devices, failure is not uncommon. One of the primary causes of implant failure is implant-associated infections (IAI).[2] In the field of orthopaedics, approximately 1–2% of joint replacement arthroplasties result in IAI.[3] The IAI rate is significantly higher in the periodontal field, with peri-implantitis seen in as many as 1 in 3 patients.[4] Infections involving fungal pathogens are emerging in both of these clinical fields, and *Candida* species are detected in as many as 90% of fungal IAI cases.[5] *Candida albicans* represents the most common fungal threat, but other notable species include *Candida parapsilosis, Candida tropicalis,* and *Candida glabrata*.[5d] In polymicrobial biofilms, *C. albicans* can protect *Porphyromonas gingivalis* from adverse conditions[6] and promote drug resistance in *Staphylococcus aureus*.[7] Its common occurrence in IAI can be attributed to the fact that *C. albicans* is found amongst the normal skin microbiota as a commensal microbe, and can occasionally translocate from the skin to the implanted device during surgery.[8] In a subset of the population, such as diabetics or those who have an otherwise compromised immune system, *C. albicans* can switch from its normal commensal state to an opportunistic pathogen. This is of particular concern because once a fungal infection becomes systemic, it is associated with a mortality rate of up to 50%.[9] In systemic candidiasis, the kidney is one of the primary organs to be affected, commonly leading to renal failure.[10] As a fungal pathogen, the virulence mechanisms of *C. albicans* differ from bacterial pathogens. One striking difference is the ability of pathogenic fungi to reversibly switch between two alternate phenotypes–an ovoid-shaped yeast phenotype and a filamentous hyphal phenotype, and this process is referred to as morphogenesis.[11] The yeast phenotype is associated with initial surface colonization, and later dissemination. The hyphal phenotype acts as structural support and promotes tissue invasion.[12] Invasion of host tissue allows *C. albicans* to enter the bloodstream and translocate around the body. Within the bloodstream, the presence of serum and the slightly alkaline pH provides ideal conditions for hyphal cell growth, which then allows the pathogen to invade

A. Hayles, R. Bright, J. Wood, D. Palms, K. Vasilev[+]
Academic Unit of STEM
University of South Australia
Mawson Lakes, Adelaide, South Australia 5095, Australia
E-mail: krasi.vasilev@flinders.edu.au
P. Zilm
Adelaide Dental School
University of Adelaide
Adelaide, South Australia 5005, Australia
T. Brown, D. Barker
Corin Australia
Baulkham Hills, New South Wales 2153, Australia
The ORCID identification number(s) for the author(s) of this article can be found under https://doi.org/10.1002/admi.202102353.

© 2022 The Authors. Advanced Materials Interfaces published by Wiley-VCH GmbH. This is an open access article under the terms of the Creative Commons Attribution License, which permits use, distribution and reproduction in any medium, provided the original work is properly cited.

[+]Present address: College of Medicine and Public Health, Flinders University, Bedford Park 5042, South Australia

DOI: 10.1002/admi.202102353

Check for updates
21967350, 2022, 12, Downloaded from https://onlinelibrary.wiley.com/doi/10.1002/admi.202102353 by Eddie Koiki Mabo Library, Wiley Online Library on [01/03/2023]. See the Terms and Conditions (https://onlinelibrary.wiley.com/terms-and-conditions) on Wiley Online Library for rules of use; OA articles are governed by the applicable Creative Commons License

host tissue at sites distal to its initial colonization.[8] *C. albicans* is highly adaptive to a range of environmental niches which is why systemic candidiasis involves such aggressive pathogenesis, leading to high rates of morbidity and mortality.

When *C. albicans* colonizes an implanted device, it forms a biofilm with a sequence of stages.[5a] Yeast cells act as initial colonizers by attaching to the surface. Surface sensing mechanisms trigger *C. albicans* to switch to the hyphal phenotype, and the polymorphic surface colony begins to secrete an extracellular matrix containing hydrolytic enzymes aiding tissue invasion.[13] Compared to their planktonic counterparts, *C. albicans* biofilm displays enhanced virulence-associated characteristics and antifungal drug resistance.[14] Biofilm associated drug resistance is influenced by multiple factors, including the architecture of biofilm, the protective extracellular matrix, and the induced expression of resistance genes such as drug efflux pumps.[8] Once biofilm cell density becomes greater than 10^6 colony forming units per milliliter (CFU mL^{-1}), yeast cells begin to disseminate and relocate to uninhabited surfaces.[15]

As a fungal species, *C. albicans* is not susceptible to the antibacterial prophylaxis that is typically used during surgical implant placement.[2b] Furthermore, the eradication of bacteria by prophylactic antibiotics can promote the necessary conditions for *C. albicans* to switch from commensalism to opportunism.[5d] To complicate matters, the eukaryotic nature of *C. albicans* makes it exceedingly difficult to treat, as there are relatively few pathogen-specific targets for drugs to be developed against.[9,16]

Recently, there has been much attention on biomaterials with engineered surface topographies which can inhibit microbial colonization.[17] These types of biomaterials are particularly attractive due to the mechanical nature by which they passively kill pathogens [18] and can be described as 'mechano-bactericidal'. Depending on the fabrication method, antimicrobial nanostructured surfaces can be engineered to consist of highly ordered and geometrically defined features[17d], or randomly oriented and heterogenous features.[19] Typically, methods that generate highly ordered nanostructures are difficult to produce on large surface areas or on objects with complex geometry, making large-scale manufacture challenging.[20] Hydrothermal etching is a highly scalable technique that generates randomly oriented nanoscale protrusions cost-effectively, with a total surface coverage irrespective of the geometric complexity of the object.

Nanostructured antimicrobial surfaces do not release any biocidal compounds, reducing the probability of cytotoxicity to surrounding tissue. Nanostructured surface modification can be emulated on common biomedical materials such as titanium and may reduce the need for prolonged drug usage and invasive revision surgeries. This is an attractive outcome because prolonged use of antifungal drugs is associated with substantial toxicity [21] and increased rates of drug resistance,[22] while revision surgeries carry the added risk of morbidity and mortality, and further increase the susceptibility to infection.[23] There has been an abundance of in vitro data to show that biomimetic, nanostructured antimicrobial surfaces are effective at killing both Gram-negative and Gram-positive bacterial pathogens, but research into their antifungal capacity is lacking. A successful anti-infective implantable biomaterial will ideally be resistant to both bacterial and fungal pathogens. Therefore, the aim of the present study was to take an established biomimetic nanostructured antimicrobial surface[24] and investigate its antifungal potential. We also evaluate whether these surfaces affect the sensitivity of the pathogen to the antifungal drug amphotericin B (AmB) (**Scheme 1**).

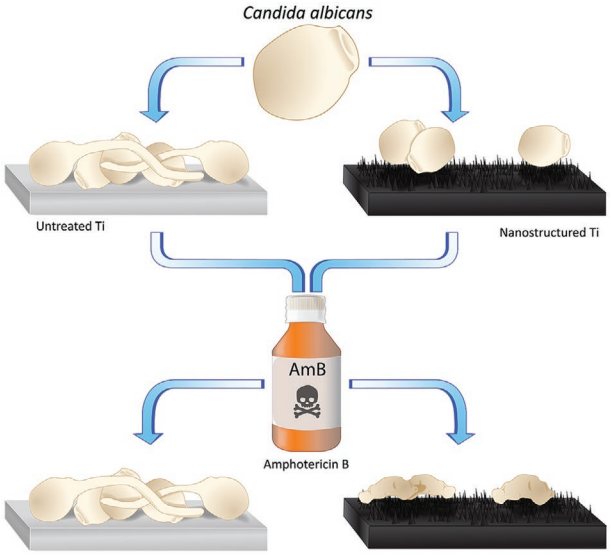

Scheme 1. Spiked titanium nanostructures inhibit fungal morphogenesis and biofilm formation, leading to an increased sensitivity to the antifungal drug amphotericin B.

2. Results and Discussion

2.1. Surface Characterization of Hydrothermally Etched Titanium (HTE-Ti)

To achieve the desired surface nanoarchitecture, Ti6Al4V alloy discs were processed by an alkaline hydrothermal treatment. This resulted in disordered, nanoscale protrusions (nanospikes) with a high aspect ratio and an approximately perpendicular orientation. The as-received titanium (AR-Ti) and HTE-Ti surfaces were imaged at high magnification under a scanning electron microscope (SEM; **Figure 1**). The AR-Ti samples (Figure 1A-C) were observed to have some pits and marks at both the microscale and nanoscale, resultant from the machining and polishing processes undertaken during manufacturing. The higher magnification SEM images of the HTE-Ti surface (Figure 1D-F) revealed the presence of hierarchically ordered sharp nanospikes. The nanospikes had a mean height of 348 ± 152 nm and a mean width at mid-height of 98 ± 60 nm. The mean spacing between neighbouring spike tips was 437 ± 46 nm. Nanoscale roughness of the AR-Ti and HTE-Ti was analyzed by atomic force microscopy (AFM) (Figure 1G and H, respectively). The AR-Ti surface was relatively smooth with an average roughness value of S_a = 4.15 nm. By contrast, the HTE-Ti surface had an average roughness value of S_a = 175.5 nm, which reflects the change in surface topography generated by the hydrothermal etching process. The water contact angle of the AR-Ti and HTE-Ti surface was 61° ± 8° and below 10°, respectively (Figure 1I,J). It is generally accepted that the increased wettability is an important property

© 2022 The Authors. Advanced Materials Interfaces published by Wiley-VCH GmbH

21967350, 2022, 12, Downloaded from https://onlinelibrary.wiley.com/doi/10.1002/admi.202102353 by Eddie Koiki Mabo Library, Wiley Online Library on [01/03/2023]. See the Terms and Conditions (https://onlinelibrary.wiley.com/terms-and-conditions) on Wiley Online Library for rules of use; OA articles are governed by the applicable Creative Commons License

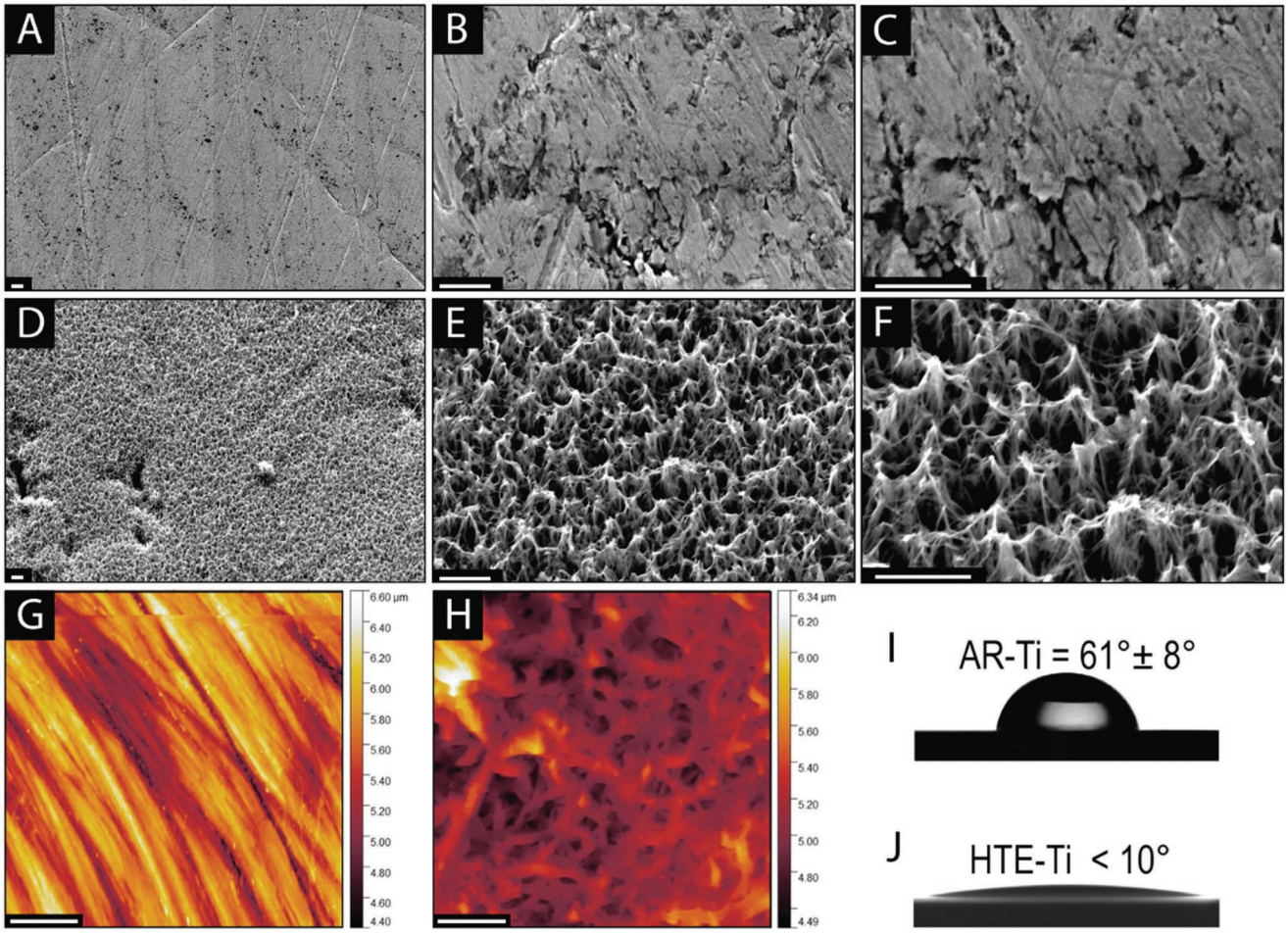

Figure 1. Representative SEM micrographs of AR-Ti A–C) and HTE-Ti D–F). Nanoscale roughness of AR-Ti G) and HTE-Ti H) measured by AFM. Static water contact angle of AR-Ti I) and HTE-Ti J) measured by the sessile drop method. Scale bars represent 1 µm.

for titanium implants because it promotes protein adsorption, host cell attachment, proliferation, and differentiation, all of which are precursors to bone formation.[25]

2.2. SEM Analysis of *C. albicans* on AR-Ti and HTE-Ti Surfaces

To determine whether HTE-Ti nanostructures could disrupt the typical morphology of a fungal pathogen, *C. albicans* was incubated in hyphae-inducing conditions on both the AR-Ti and HTE-Ti surfaces (**Figure 2**). On the AR-Ti surface (Figure 2A-C), *C. albicans* was observed in both its yeast and hyphae forms, with typical dense hyphal networks containing clusters of yeast cells. In contrast, on the HTE-Ti surface (Figure 2D-F), *C. albicans* was primarily observed in its yeast cell phenotype. Where hyphae were observed, their morphology appeared disturbed, and their length was stunted. Figure 2E shows a hyphal apex sunken into the nanostructure, likely affecting its capacity to elongate. In Figure 2F, a hyphal cell appeared shriveled and fragmented. These hyphae can be compared against the healthy hyphal cells shown in Figure 2A-C, which appear turgid, longer, and more networked. Despite the disturbed hyphal morphology on the HTE-Ti surface, yeast cells typically appeared healthy, however an exception to this was seen in Figure 2F which shows two atypical appearing yeast cells.

2.3. *C. albicans* Viability, Morphogenesis, and Growth Rate on HTE-Ti

C. albicans cells attached to AR-Ti and HTE-Ti were stained with *Bac*Light LIVE/DEAD and imaged with a CLSM following 48 h incubation (**Figure 3**). On the AR-Ti surface (Figure 3A) there was clear evidence of a dimorphic colony of cells, with networks of hyphae surrounded by yeast cells. On the HTE-Ti surface (Figure 3B), the cells were almost exclusively in the yeast form. Few hyphae were observed on the HTE-Ti surface (enlarged image), and they appeared stunted in length. The cells on both surfaces fluoresced green indicating that the cell membrane had not been ruptured by the HTE-Ti surface.

Vertically stacked fluorescence images were used to generate 3-D models of *C. albicans* on the AR-Ti and HTE-Ti surfaces to reveal the spatial arrangement of cells (Figure 3C,D). Cells on the AR-Ti surface were more likely to aggregate vertically, particularly surrounding hyphal networks. Morphogenesis was compared across both surfaces (Figure 3E), and the

© 2022 The Authors. Advanced Materials Interfaces published by Wiley-VCH GmbH

21967350, 2022, 12, Downloaded from https://onlinelibrary.wiley.com/doi/10.1002/admi.202102353 by Eddie Koiki Mabo Library, Wiley Online Library on [01/03/2023]. See the Terms and Conditions (https://onlinelibrary.wiley.com/terms-and-conditions) on Wiley Online Library for rules of use; OA articles are governed by the applicable Creative Commons License

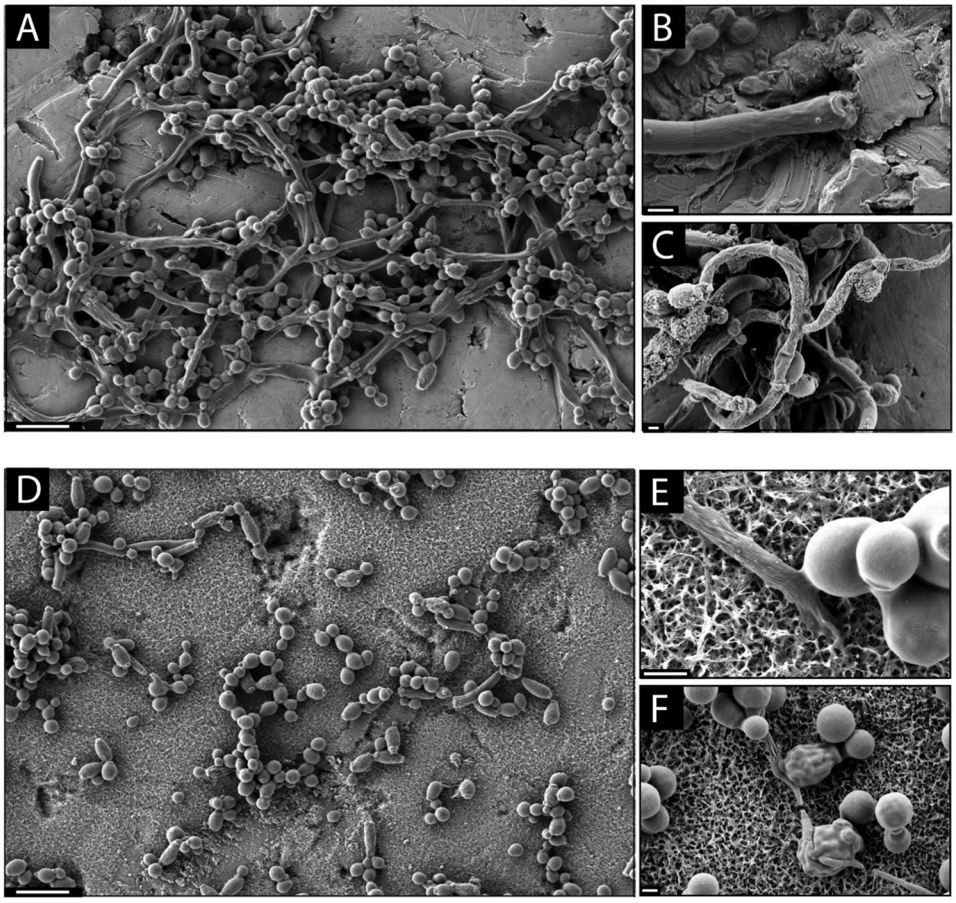

Figure 2. SEM micrographs showing *C. albicans* incubated on AR-Ti A–C) and HTE-Ti D–F). Scale bars represent 10 µm on A and D, and 1 µm for B, C, E, F.

mean hyphae percentage, length, and network size on the HTE-Ti surface were plotted as a reduction from the values obtained on the AR-Ti surface. It was observed that there was a 91% reduction in hyphae percentage, a 30% reduction in hyphae length, and 85% reduction in hyphal network size on the HTE-Ti surface. By having smaller hyphal networks and an overall reduced presence of hyphae, it is likely that *C. albicans* colonizing the HTE-Ti surface is less structurally robust and potentially less resistant to antifungal drugs.[26] Consequently, the fungus may be more susceptible to host clearance and antifungal treatment. Furthermore, the reduced hyphal length is an important observation, as long hyphae are known to be better equipped to form multiple points of adhesion to host cells, increasing their capacity for invasion and systemic dissemination.[27]

Biovolume was compared across both surfaces using 3D fluorescence images (Figure 3F) following 48 h incubation. It was found that the biovolume on HTE-Ti was approximately 50% lower compared to the AR-Ti surface. To determine whether the nanostructured surface would also contribute to a reduced rate of growth over longer time periods, colony enumeration was performed at 4 timepoints over 10 days (Figure 3G). After 24 h, the cell density on the HTE-Ti surface was reduced by 1-log compared to the AR-Ti surface (approximately 10^6 and 10^7 CFU cm^{-2}, respectively). At this point during the incubation, the cell density was still relatively low, and cells must face the challenge of dividing laterally across the surface. The observed decrease in cell density at the early timepoints is likely a consequence of the mechanical interactions between cells and the nanostructured surface, which may have reduced the capacity for cell elongation. Over the following 10 days, the cell density on the AR-Ti surface remained relatively stable, only increasing slightly to 5.1×10^7 CFU cm^{-2} at day 10. Over the same period, the cells on the HTE-Ti surface gradually accumulated up to a peak of 2.7×10^7 CFU cm^{-2}. This was still a statistically significant reduction from the AR-Ti surface ($P < 0.001$). At these later timepoints, cells may be accumulating vertically such that the cells in the upper layers escape from the influence of the nanostructure. This could explain why the cell density on the HTE-Ti surface was able to approach similar values to the AR-Ti surface toward the end of the 10-day incubation period. Despite this, the reduced cell density on HTE-Ti at day 10 suggests that there are factors other than the mechanical interaction with the nanostructured surface which affect cell accumulation on the HTE-Ti surface. It has been shown that mutant *C. albicans* which cannot form hyphae are also unable to form a strong biofilm.[12b] Hyphal cells enable thicker biofilms, and they function as structural support for the surrounding yeast cells.[27a] The relative lack of hyphal cells observed on the HTE-Ti surface may consequently explain the reduced cell density, as it

© 2022 The Authors. Advanced Materials Interfaces published by Wiley-VCH GmbH

21967350, 2022, 12, Downloaded from https://onlinelibrary.wiley.com/doi/10.1002/admi.202102353 by Eddie Koiki Mabo Library, Wiley Online Library on [01/03/2023]. See the Terms and Conditions (https://onlinelibrary.wiley.com/terms-and-conditions) on Wiley Online Library for rules of use; OA articles are governed by the applicable Creative Commons License

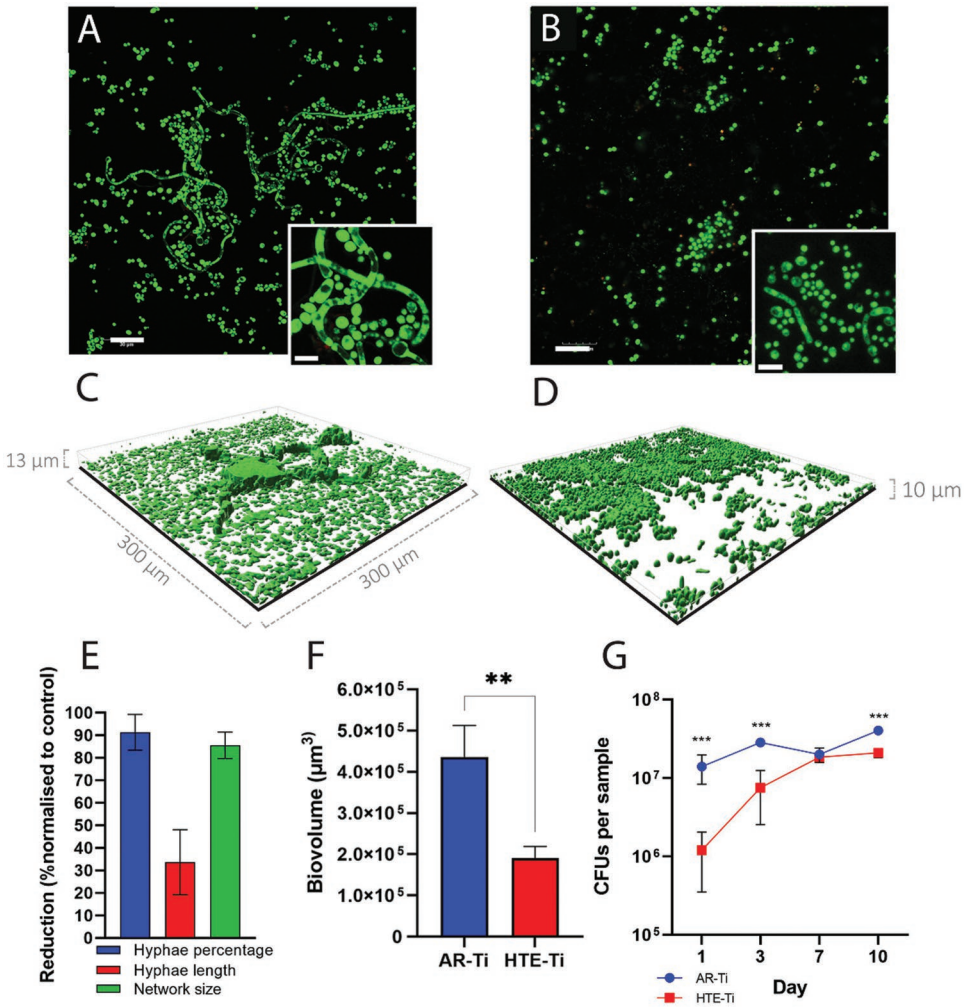

Figure 3. Single plane fluorescence micrographs showing differences in cell morphology on AR-Ti and HTE-Ti at the interface of the surface A,B); 3-D representations of *C. albicans* cultured on AR-Ti and HTE-Ti C,D); morphological statistics E); biovolume F) and longitudinal rate of surface colonization G). Mean ± SD, $n = 3$, ** $p < 0.01$. ***$p < 0.001$

is likely that a robust biofilm could not be formed even after 10 days.

2.4. FIB-SEM Cross-Sectional Analysis

To further characterize the mechanical interaction between *C. albicans* cells and HTE-Ti, FIB cross-sections of the cell-surface interface were generated, which were then imaged by SEM (**Figure 4**). In Figure 4A, a typical yeast cell is shown attached to the smooth AR-Ti surface. The yeast cell appeared turgid, and its inner membrane appeared smooth. In Figure 4B, two yeast cells in the process of budding, are shown (labelled 1 and 2) attached to the HTE-Ti surface. Cell 1 had a typical appearance, and its morphology was smooth and turgid. Cell 2 had a shriveled and flaccid appearance. A cross-section of these two cells is shown in Figure 4C. The dashed circles highlight points at which the nanostructure appeared to physically deform the cell wall. Both cells 1 and 2 had a rough, bumpy inner membrane surface which was strikingly different from the cell on the AR-Ti surface in Figure 4A. It is interesting to note that although cell 1 was turgid and superficially undisturbed, its inner membrane surface was still clearly deformed compared to the cell on the AR-Ti surface. Similar observations were made for hyphal cells. In Figure 4D, a hyphal cell is severely warped against the nanostructure beneath it. The cell membrane of the hyphal cell was observed to be much thinner in regions in direct contact with the nanostructure. This contrasts the hyphae on AR-Ti, which were shown to be resting flat against the surface without any obvious deformation (Figure 4E). Despite the membrane disturbances highlighted by cross sectional analysis, there was no evidence of membrane penetration or rupture by the HTE-Ti nanostructure.

C. albicans has an arsenal of responses which are triggered by various stressors, such as pH, temperature, or in this case, cell wall stress.[28] In particular, *C. albicans* attempts to remediate cell wall stress by fortifying its chitin layer (the structural component of the cell wall).[29] Further, the same response results in a reduced ability for dividing *C. albicans* cells to separate, which may account for the reduction in viable cell counts presented in Figure 3. Cell wall stress also interferes with the

© 2022 The Authors. Advanced Materials Interfaces published by Wiley-VCH GmbH

21967350, 2022, 12, Downloaded from https://onlinelibrary.wiley.com/doi/10.1002/admi.202102353 by Eddie Koiki Mabo Library, Wiley Online Library on [01/03/2023]. See the Terms and Conditions (https://onlinelibrary.wiley.com/terms-and-conditions) on Wiley Online Library for rules of use; OA articles are governed by the applicable Creative Commons License

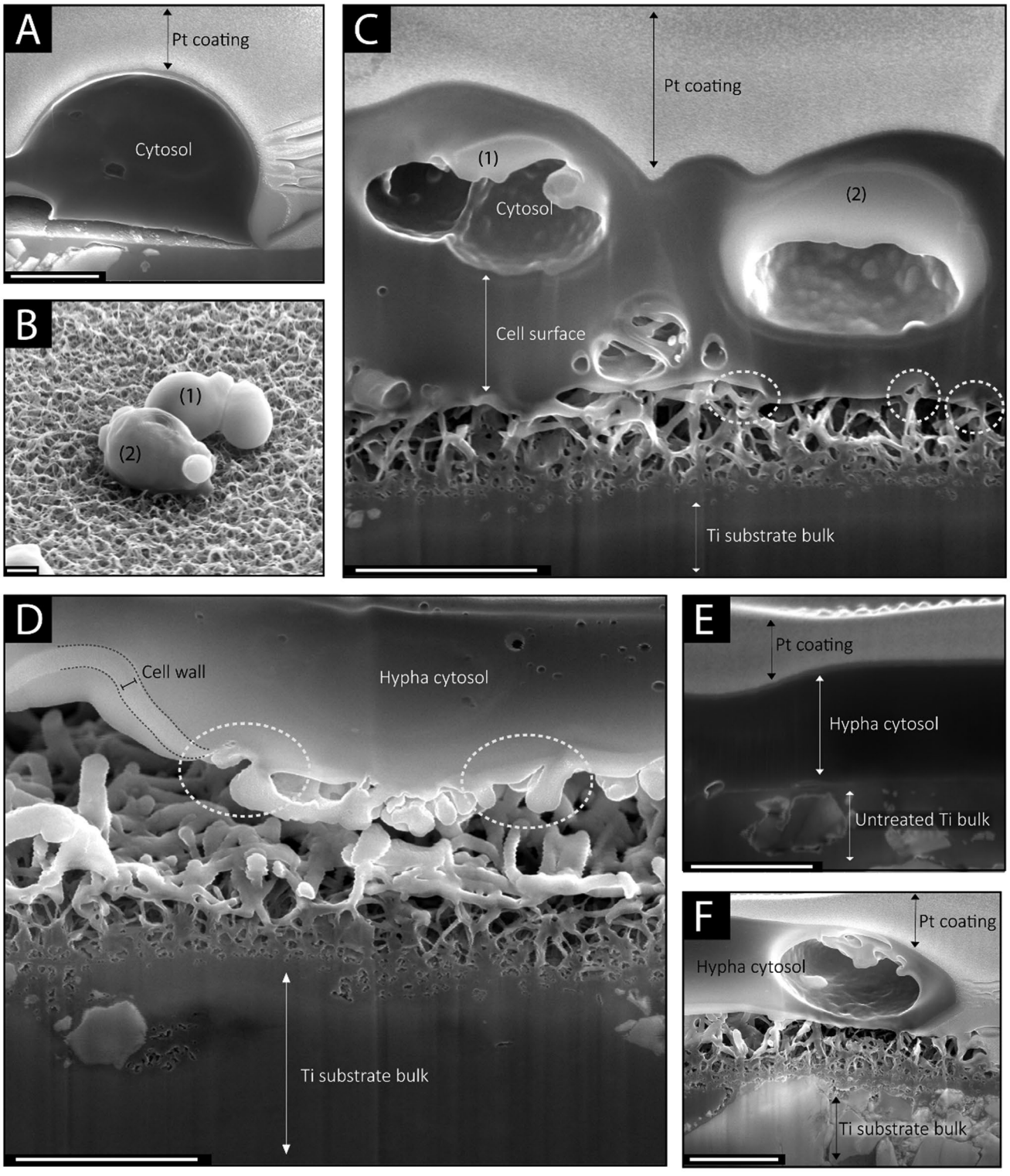

Figure 4. FIB-SEM analysis of *C. albicans* yeast cells on AR-Ti A) and HTE-Ti B,C), and hyphal cells on AR-Ti (E) and HTE-Ti D,F). Dashed circles highlight points of cell wall deformation at the cell-nanostructure interface. Scale bars represent 1 µm.

localization of septin.[30] One of the functions of septin is to initiate and mediate proper hyphal morphogenesis and regulate their shape.[31] This therefore may be the key reason for the observed inhibition in hyphal morphogenesis.

© 2022 The Authors. Advanced Materials Interfaces published by Wiley-VCH GmbH

21967350, 2022, 12, Downloaded from https://onlinelibrary.wiley.com/doi/10.1002/admi.202102353 by Eddie Koiki Mabo Library, Wiley Online Library on [01/03/2023]. See the Terms and Conditions (https://onlinelibrary.wiley.com/terms-and-conditions) on Wiley Online Library for rules of use; OA articles are governed by the applicable Creative Commons License

21967350, 2022, 12, Downloaded from https://onlinelibrary.wiley.com/doi/10.1002/admi.202102353 by Eddie Koiki Mabo Library, Wiley Online Library on [01/03/2023]. See the Terms and Conditions (https://onlinelibrary.wiley.com/terms-and-conditions) on Wiley Online Library for rules of use; OA articles are governed by the applicable Creative Commons License

2.5. Relative Gene Expression of Hyphae-Associated Virulence Factors

Based on the previous observations of inhibited morphogenesis, it was hypothesized that the expression of hyphae-associated virulence factors may also be altered on the HTE-Ti surface. To investigate this, *HWP1, ALS3,* and *SAP5* were chosen as hyphae-associated genes of interest to be measured by qPCR (**Figure 5**). *HWP1* encodes Hyphal wall protein 1 (Hwp1), a surface protein which has roles in cell wall assembly, development of hyphae, adhesion, and invasion of host cells.[32] Hwp1 enables *C. albicans* hyphae to covalently bond with host cells, promoting strong adhesion prior to invasion.[8] It is also critical to biofilm formation, and Hwp1-null mutants are incapable of forming biofilm in vivo.[12b,33] In an in vitro model, a Hwp1-deficient mutant formed a yeast-only biofilm while the surrounding media contained both yeast and hyphae.[12b] This emphasizes the hypha-specific adhesive role of Hwp1. Agglutinin-like sequence 3 (Als3), encoded by *ALS3,* is another hyphae-associated surface protein that has adhesin functions and is central to biofilm formation.[6,12b,33–34] However, unlike Hwp1, Als3 is not a requirement for biofilm formation in vivo.[12b] Als3 and Hwp1 are said to be complementary in function, and Als3 interacts with Hwp1 to contribute to biofilm formation.[33b] Secreted aspartyl proteinase 5 (Sap5) is a hyphae-associated protein, encoded by the *SAP5* gene, which hydrolyses host proteins and enables invasion of host cells.[6,8,35] *SAP5* is coregulated with hypha formation and is a requirement for hyphae to invade parenchymal organs.[35b]

In the present study, we measured the relative mRNA transcription of hyphae-associated genes from *C. albicans* incubated on AR-Ti and HTE-Ti samples. Based on preliminary observations we noted that the hyphae phenotype was absent when *C. albicans* was cultured in media without serum supplementation—therefore we have included a no-serum group as a control to establish baseline levels of gene expression of the three genes. As the presence of serum is a contributing factor to hyphae formation, it was expected that the chosen genes would be upregulated when exposed to serum. Our observations support this assumption. However, the transcriptional response of *C. albicans* cultured on the HTE-Ti surface differed from that cultured on AR-Ti. For *HWP1,* serum treatment induced an upregulation 1040% on the AR-Ti surface, but only 380% on the HTE-Ti surface after 48 h. This correlates well with the observation that morphogenesis was substantially impeded on the HTE-Ti surface. For *ALS3,* the presence of serum did not result in a statistically different mRNA level between surfaces. However, the biofilm-promoting contribution of Als3 is likely impeded on the HTE-Ti surface because there is less Hwp1 for it to interact with.[33b] This interpretation would explain why the colony enumeration results yielded significantly fewer counts on HTE-Ti compared to the AR-Ti surface. For *SAP5,* serum supplementation resulted in a 260% increase in mRNA on the AR-Ti surface, and a 360% increase on the HTE-Ti surface. This could be interpreted as an adaptive response to mechanically induced stress. Other stressors are known to induce an upregulation of *SAP5,* such as antifungal treatment [36], or phagocytosis by macrophages.[35b] A common mechanism may be responsible for the increased *SAP5* expression of *C. albicans* on HTE-Ti as well as within the phagosome of a macrophage. Within the phagosome, the macrophage attacks pathogens with reactive oxygen species (ROS) to generate lethal oxidative stress.[37] ROS has also been shown to be involved in the bactericidal activity of HTE-Ti,[38] and it is believed that ROS is generated intracellularly as a downstream effect of membrane perturbation.[39] It is plausible that *C. albicans* incubated on the HTE-Ti surface is induced to generate sublethal levels of ROS, and that this exposure triggers it to upregulate *SAP5*. It was also noted that in the absence of serum, *ALS3* and *SAP5* showed reduced expression on the HTE-Ti surface compared to AR-Ti. However, as the context of this study focuses on HTE-Ti as a prospective implantable biomaterial which would encounter serum, this observation bears little relevance. Overall, the expression profile of the targeted genes was indicative of a stressed fungal culture with a reduced ability to form a typical biofilm.

2.6. Antifungal Sensitivity of *C. albicans* Cultured on HTE-Ti

Spurred by the observed inhibition of morphogenesis, biofilm formation, and modulation in gene expression, we hypothesized that *C. albicans* cultured on HTE-Ti would be more susceptible to clearance by antifungal drugs. To investigate this, the fungicidal polyene, AmB, was administered daily at a concentration of 20 μg ml^{-1} for 7 days against 3-day established cultures of *C. albicans* on AR-Ti and HTE-Ti. By design, our experimental approach was to investigate substantially lower doses than what might be used clinically. When AmB is administered intravenously in a clinical setting, serum concentrations typically reach 250 μg ml^{-1}.[40] AmB is currently considered the gold-standard in antifungal treatment [41] and is therefore a highly relevant drug to gain insights into potential clinical outcomes. On the AR-Ti surface, AmB did not cause a reduction in biofilm thickness, but did decrease the overall biovolume by approximately 70% over the first 5 days. However, by day 7 the pathogen began to recover to almost the same biovolume at which it started (**Figure 6**A-D). Supporting this observation, the proportion of dead biovolume was approximately 12–14% in the first 5 days, but on day 7 it was reduced to only 7% (Figure 6C). This suggests that the fungus had become somewhat resistant to the presence of AmB when cultured on the AR-Ti surface. *C. albicans* is known to be highly adaptive to hostile conditions, and acquired tolerance to antifungal drugs has been observed to occur in as little as 2 h.[42] When cultured on HTE-Ti, *C. albicans* was substantially more sensitive to AmB (Figure 6B), and after the first day of AmB treatment, the proportion of dead biovolume was 40%, which increased over the 7 days until the entire culture was eradicated (Figure 6C). This was met by a proportionate decline in thickness. Similarly, the total biovolume present on the HTE-Ti surface progressively dissipated over the 7 days of treatment and did not recover as it did on the AR-Ti surface (Figure 6D).

The dramatic difference in the sensitivity of *C. albicans* to AmB on AR-Ti and HTE-Ti resonates well with the observed morphological changes between cultures incubated on these two surfaces as well as the gene expression analysis. In general,

© 2022 The Authors. Advanced Materials Interfaces published by Wiley-VCH GmbH

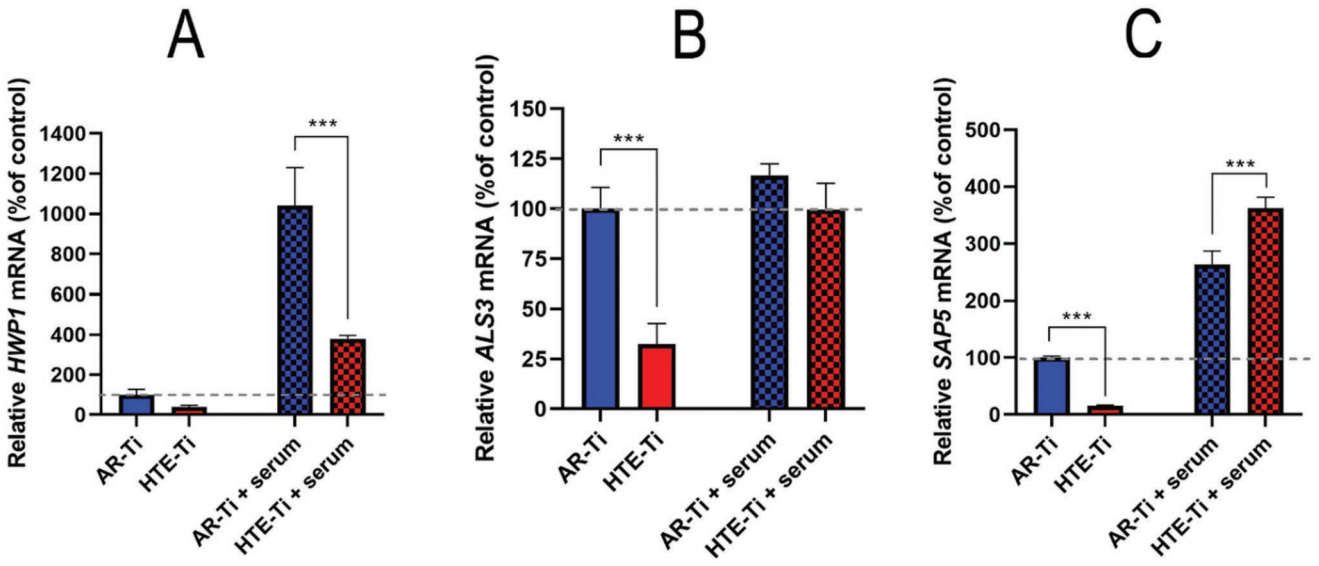

Figure 5. Relative mRNA levels of hyphae-associated virulence factors of *C. albicans* incubated on HTE-Ti at 48 h. A) *HWP1*, B) *ALS3*, C) *SAP5*. Mean ± SD, $n = 3$. *** $p < 0.001$.

microbial biofilms can increase antibiotic tolerance up to 1000x, in part due to the protective effects of EPS, expression and transmission of resistance genes and plasticity of metabolic state.[43] For *C. albicans* specifically, its tolerance to antifungals is granted by multiple factors. First, *Candida* biofilms have a high cell density, and it has been shown that high cell densities

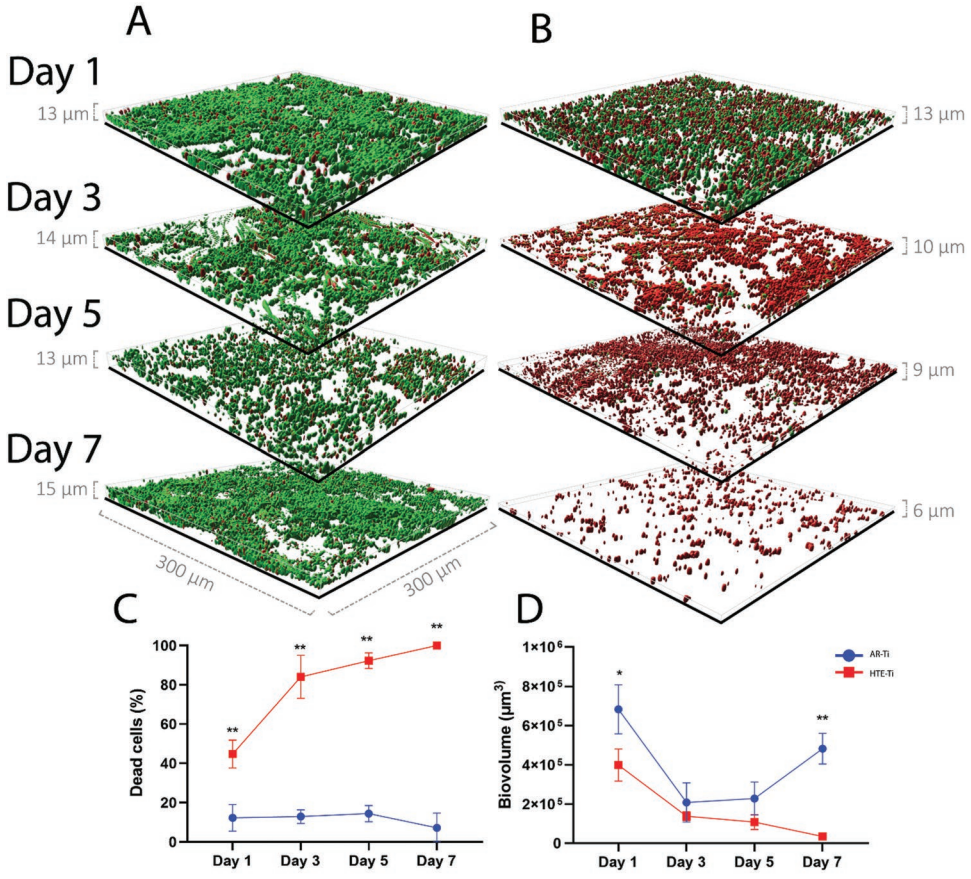

Figure 6. Fluorescence microscopy models of *C. albicans* treated with AmB and incubated on AR-Ti A) and HTE-Ti B). Proportions of live and dead cells over 7 days of treatment C). Progressive change in total measured biovolume D). Mean ± SD, $n = 3$ **$p < 0.01$, *$p < 0.05$

© 2022 The Authors. Advanced Materials Interfaces published by Wiley-VCH GmbH

21967350, 2022, 12, Downloaded from https://onlinelibrary.wiley.com/doi/10.1002/admi.202102353 by Eddie Koiki Mabo Library, Wiley Online Library on [01/03/2023]. See the Terms and Conditions (https://onlinelibrary.wiley.com/terms-and-conditions) on Wiley Online Library for rules of use; OA articles are governed by the applicable Creative Commons License

increase the concentration of AmB required to inhibit growth, even in the planktonic form.[44] Beyond this, filamentous forms of *C. albicans* have been shown to be substantially more resistant to AmB-induced programmed cell death compared to their yeast counterparts.[45] It is unsurprising then that filamentous-defective mutants of *C. albicans* have been shown to be sensitized to AmB.[44] In the present study, *C. albicans* cultured on HTE-Ti was shown to have a lower cell density and substantially reduced filamentation, and these two factors likely explain the observed increase in sensitivity to AmB. Further, AmB functions by binding to ergosterol in the plasma membrane, thereby creating pores and disrupting membrane integrity.[42] It is plausible then that the membrane perforation induced by AmB acts synergistically with the cell wall perturbation which has been shown to be associated with nanostructured antimicrobial surfaces.[46] A similar occurrence has been reported, in which cell wall stress increases *C. albicans* sensitivity to the antifungal drug nikkomycin.[47]

3. Outlook

Recently there has been a substantial focus directed toward the fabrication of anti-infective biomaterials.[48] Biomaterials can be rendered anti-infective using two main fabrication strategies. One strategy involves the elution of antibacterial or antifungal drugs, including various metals such as silver. The benefit of this strategy is that it can eliminate pathogens not only on the surface of the device but also in the proximal tissue. However, there are always concerns associated with eluting materials and coatings associated with tissue toxicity. Furthermore, the reservoir of eluted compounds would eventually be exhausted.[49] The alternative strategy involves generating a hostile surface which directly kills pathogens on contact. Nanostructured antimicrobial surfaces take the latter approach, and various laboratories have fabricated these biomaterials with impressive antibacterial efficacy.[17d,38,50] These surfaces kill bacteria through physical interaction rather than by a chemical eluting mechanism,[18,51] which means their efficacy should not decrease over time.[52] Further supporting this notion, we incubated *C. albicans* for 10 days on the HTE-Ti surface, then detached the cells by vortex and analyzed the nanostructure by SEM (Figure S4, Supporting Information). We noted that the long-term fungal culture did not affect the integrity of the nanoscale architecture, suggesting that the nanostructure could remain effective long-term. This is reassuring, as *Saccharomyces cerevisiae* yeast cells have been shown to shear off the nanopillars found on cicada wings.[53]

Fungal pathogens are particularly difficult to treat. Due to their eukaryotic nature, it is difficult to develop drugs which target the pathogen and not the host. This has become increasingly complicated by the emergence of drug resistance against existing treatments. Furthermore, the ability of *C. albicans* to form a robust polymorphic biofilm allows it to better resist antifungal treatment.[54] Recently, attention has been directed toward targeting the virulence mechanisms of fungal pathogens.[16,55] In this way, the aim is not to directly kill the fungal invader, but to limit its capacity to cause systemic infection. One such strategy is to impede *C. albicans* from switching phenotype and forming a polymorphic biofilm[55] In the case of implanted devices, *C. albicans* cannot form a strong biofilm if morphogenesis is impeded.[12b] This may limit its invasiveness and facilitate clearance of the pathogen by the host immune system.

Due to the hostile nature of HTE-Ti toward both bacteria and fungi, it is prudent to assess the cytocompatibility of the modified surface with mammalian cells before the technology can be elevated beyond in vitro studies. In a previous study, we have demonstrated that HTE-Ti does not reduce the viability of human dermal fibroblasts.[24] Similarly, in the present study, we showed that murine macrophages were able to grow unimpeded on HTE-Ti, without any loss in viability (Figure S5, Supporting Information).

The aim of the present study was to take a biomimetic surface which has already been characterized as antibacterial and assess its capacity to inhibit a clinically relevant fungal pathogen. With that goal, we have determined that the HTE-Ti surface does not outright kill *C. albicans* like it kills bacteria, but instead mitigates its ability to form a robust polymorphic biofilm. This functionality is likely mediated by the mechanical interaction between the nanostructure and the fungal cell wall, which severely warps the cell but does penetrate the cytosol, as evidenced by cross-sectional analysis. In this way, the antifungal activity of HTE-Ti is distinct from the antifungal activity of the naturally occurring nanostructure found on the wing of *Neotibicen tibicen*, which ruptures fungal cells on contact.[53,56] Ultimately, the varying mechanical interaction between a cell and a nanostructure depends on both the topographical parameters of the nanostructure (i.e. structure height, diameter, aspect ratio, spacing) and the biological properties of the cell (i.e. size, cell wall thickness, motility, mode of division). These interactions have been previously reviewed in detail.[20] Fabrication parameters may be tuned to generate nanostructures with defined geometric dimensions, which has been used as a method to optimize bactericidal efficacy.[19c] In this regard, a nanostructured surface may be tuned to specialize in killing either bacteria or fungal cells. It is presently unclear whether further tuning a nanostructured surface to penetrate and kill fungal cells would result in a trade-off in bactericidal efficacy, due to the different biological properties between bacteria and fungi. Nevertheless, it is highly encouraging that the results presented here are indicative of a broad-acting nanostructure, which both kills bacteria on contact, and inhibits polymorphic fungal biofilm. This is clinically important, as a sufficiently effective antimicrobial biomaterial must inhibit both fungal and bacterial pathogens.

By inhibiting fungal biofilm, the function of the HTE-Ti surface can be compared to the recent observations made by Ivanova and colleagues,[57] who showed that the nanostructured wings of the Damselfly repel fungal cells. Although the biofilm inhibiting effect is similar between the Damselfly wing and HTE-Ti, their mechanisms are quite different. The Damselfly wing is a hydrophobic surface which entraps a layer of air between nanopillars, and this air layer reduces the propensity for fungal cells to attach to the surface.[57] The HTE-Ti surface is highly hydrophilic and thus there can be no trapped air to exert this effect. The biofilm inhibition observed on HTE-Ti is therefore more attributable to the mechanical interactions between the fungus and the nanostructures. Furthermore, we found that

© 2022 The Authors. Advanced Materials Interfaces published by Wiley-VCH GmbH

21967350, 2022, 12, Downloaded from https://onlinelibrary.wiley.com/doi/10.1002/admi.202102353 by Eddie Koiki Mabo Library, Wiley Online Library on [01/03/2023]. See the Terms and Conditions (https://onlinelibrary.wiley.com/terms-and-conditions) on Wiley Online Library for rules of use; OA articles are governed by the applicable Creative Commons License

the reduced presence of robust biofilm enhances the capacity for fungicidal drugs to eliminate the surface culture in vitro. This suggests that HTE-Ti biomaterials could potentially reduce the burden of fungal pathogens by impeding them sufficiently for the host immune system and/or antifungal drugs to effectively clear them in a real clinical setting. While the results in this study are highly encouraging, they are limited by the constraints of the in vitro experiment. It is yet to be determined how effective the surface would be at inhibiting fungal biofilms within the dynamic biological environment of a mammalian host, and future in vivo studies will be of great importance in bringing this technology forward for clinical translation.

4. Conclusion

In the present study, we investigated the capacity of a nanostructured antimicrobial surface containing sharp protrusions to inhibit the fungal pathogen *C. albicans*. SEM analysis revealed that morphogenesis was severely impeded, as primarily yeast cells were observed on the HTE-Ti surface. This contrasts with the AR-Ti surface, which showed high density networks of hyphae. Quantification of morphogenesis showed a significant reduction in hyphal percentage, length, and network size. Fluorescence images revealed that *C. albicans* had not been ruptured by the nanostructured surface, but cross-sectional analysis confirmed significant cell wall disturbance. 3-dimensional fluorescence analysis revealed a reduced biovolume on the HTE-Ti surface. A longitudinal incubation resulted in a decreased rate of surface colonization, and a reduced overall accumulation of cells on the HTE-Ti surface. Relative gene expression targeting virulence-associated genes provided molecular support to the morphology and colony enumeration analyses. An impeded expression of *HWP1* supported the reduced presence of hyphae and reduced overall cell accumulation. An upregulation of *SAP5* may reflect an adaptive response to the hostile conditions, as previously seen with antifungal drugs. A 7-day fungicide treatment at sub-clinical concentrations resulted in total clearance of *C. albicans* on HTE-Ti, while it was ineffective on the AR-Ti surface. Overall, the data presented in this study indicates that HTE-Ti inhibits the capacity of *C. albicans* to form a robust biofilm by imposing severe cell wall stress and subsequently inhibiting morphogenesis and cell proliferation. This inhibition weakened the antifungal drug resistance typically associated with biofilm formation. In an in vivo situation, this may facilitate clearance of the fungal pathogen by the host immune response, as well as make the pathogen more sensitive to orally administered antifungal drugs. These are major findings towards understanding the properties of such biomimetic nanostructures and applications on medical device surfaces.

5. Experimental Section

Fabrication of Nanostructure on Ti6Al4V: As-received polished Ti6Al4V discs had a diameter of 10 mm, a height of 3 mm, and a surface area of 0.78 cm^2. The AR-Ti discs were used as the control samples. An alkaline hydrothermal treatment was used to modify the AR-Ti discs, resulting in the hydrothermally etched titanium alloy surface. Treatment was carried out in a stainless-steel reactor (Parr Instrument Company, USA). 1M KOH was used as the alkaline solution for etching, which was heated to 165 °C for 5 h. The reaction vessel was cooled down with flowing water and samples were rinsed with ultrapure water. After 2 h of air drying at 70 °C, samples were annealed inside a tubular furnace at 450 °C for 4 h and cooled overnight. Samples were cleaned, placed in autoclave bags then autoclaved at 121 °C for 20 min.

Surface Characterization of HTE-Ti: HTE-Ti surface topography was analyzed with a Zeiss Merlin FEG-SEM (Zeiss, Germany) equipped with a SE2 detector at 2KV with a 4 mm working distance, using magnifications between 5000 and 50 000*x*, with a 45° stage tilt. SEM images were imported into ImageJ v1.53 (NIH, USA) to measure nanostructure topography. The nanostructures were observed to be composed of a network of spikes which coalesced at their apex, forming a basal pane which branched into an upper layer of spikes. Nanospike height was measured by the distance between the spike apex and the basal plane. Width was determined at mid-height, using a correction factor $\frac{x}{\cos 45^\circ}$ where x equals the nanospike length, to compensate for dimensional distortion caused by the tilted stage during SEM imaging. Mean height and width of spikes were measured across 5 samples, by measuring 25 nanospikes per sample. Nanospike spacing was determined from four SEM images at 0-degree stage tilt, and the nanospike density was calculated in 25 μm^2 fields using ImageJ software v1.53a (NIH, USA). The mean spacing between nanospikes was calculated by: $\left(\frac{[\text{square root of density}]}{25\,\text{mu m}} \times 1000\right)$ to express the measurement in nm. Measurements were presented as mean and standard deviation. Atomic Force Microscopy (AFM) measurements were performed in air using a Bruker Dimension Icon. An NT-MDT NSG03 silicon nitride cantilever with a conical tip quoted by the manufacturer with a radius under 10 nm and a half side angle of 18° was used in PeakForce mode on the HTE-Ti surface. Initial calibration of the cantilever on a glass microscope slide derived a normal spring constant of 2.0 N m^{-1} and a deflection sensitivity of 94.4 nm V^{-1}. PeakForce amplitude over a 5 μm^2 image was set at 150 nm with a frequency of 2 kHz, a lift height of 34 nm, and a scan rate of 8.84 $\mu m\ s^{-1}$. Roughness values were calculated through Gwyddion data analysis software v2.54. Wettability was measured by contact angle (θ) using the sessile drop method, by a goniometer RD-SDM02 (RD Support, UK). Measurements were taken on 5 random areas over triplicate samples. The contact angle of 4 µl ultrapure water was measured by a tangent fitting method using the Contact_Angle.jar plugin for ImageJ v1.53 (NIH, USA).

Cultures and Conditions: *Candida albicans* (ATCC 10231) was retrieved from glycerol stock stored at −80 °C, and plated onto yeast extract peptone dextrose (YPD) agar plates containing 1% yeast extract, 2% bacteriological peptone, 2% sucrose, and 1.5% agar, then incubated overnight at 37 °C. An isolated colony was transferred to YPD broth and incubated overnight at 37 °C in static conditions. Following 18 h growth, the cell density was measured using a Nanodrop 2000 spectrophotometer (Thermo Scientific, MA, USA), using absorbance at 600 nm (OD_{600}). The OD_{600} was adjusted to 0.1, corresponding to approximately 1×10^7 CFU ml^{-1}.

Inoculation of C. albicans on Titanium Samples: HTE-Ti and AR-Ti discs were aseptically placed into individual wells of a 24-well plate. Diluted *C. albicans* culture was pelleted and resuspended in phosphate buffered saline (PBS) to the same volume. 50 µl containing approximately 5×10^5 CFU was pipetted onto the surface of each disc and incubated for 3 h at 37 °C to allow for cells to attach. Subsequently, 1 ml of Spider medium (1% nutrient broth, 1% peptone, 0.2% K_2HPO_4, adjusted to pH 7.2) supplemented with 20% fetal calf serum (FCS: Gibco, MA, USA), was pipetted into each well. Samples used for SEM, fluorescence microscopy, and PCR were incubated for 48 h at 37 °C on an orbital shaker (Ratek Instruments Pty. Ltd., VIC, Australia) at 90 RPM, which was sufficient for the development of a mature polymorphic biofilm.[58] For the growth rate assay, samples were incubated under the same conditions for 10 days, with analysis undertaken at days 1, 3, 7, and 10, with daily replenishment

© 2022 The Authors. Advanced Materials Interfaces published by Wiley-VCH GmbH

21967350, 2022, 12, Downloaded from https://onlinelibrary.wiley.com/doi/10.1002/admi.202102353 by Eddie Koiki Mabo Library, Wiley Online Library on [01/03/2023]. See the Terms and Conditions (https://onlinelibrary.wiley.com/terms-and-conditions) on Wiley Online Library for rules of use; OA articles are governed by the applicable Creative Commons License

of media. Samples for SEM analysis were fixed in 1.25% glutaraldehyde, 4% paraformaldehyde in PBS containing 4% sucrose. Samples for PCR analysis were immersed in 500 µl RNAlater (Invitrogen, MA, USA) and stored at −80 °C until required. Samples for fluorescence microscopy and colony enumeration were immediately analyzed after incubation.

SEM Analysis of C. albicans Morphology: AR-Ti and HTE-Ti samples for SEM analysis were chemically dehydrated according to the following steps: PBS wash (5 min), 50% ethanol (10 min), 70% ethanol (10 min), 100% ethanol (10 min), 1:1 ratio of 100% ethanol and hexamethyldisilazane (HMDS: Sigma-Aldrich, St. Louis, MO, USA) (20 min), 100% HMDS (20 min), air dry (2 h). Samples were then mounted on aluminium SEM stubs and sputter coated with 2nm platinum and imaged with a Zeiss Merlin FEG-SEM (Zeiss, Jena, Germany).

Focused Ion Beam (FIB) Milling: Titanium samples were loaded into a FEI DualBeam FIB-SEM (Thermo Scientific, MA, USA) and the system was purged to create a vacuum. Prior to cross-sectional analysis, the stage was tilted by 52°, moving the titanium discs perpendicular to the gallium ion beam, with a working distance of 4 mm. Before milling, cells of interest were coated with 1 µm of platinum using an accelerated voltage of 10 kV and a 0.46 nA current to protect morphology. Following coating, cross-sections were cut at a depth of 5 µm with an accelerated voltage of 10 kV and a 2.6 nA current, followed by a current of 0.46 nA for further refinement of cross-sections. Images of cross-section were acquired using electron beam accelerating voltages of 10 kV and current of 0.17 nA.

Live/Dead Fluorescence and Morphogenesis Quantification: Samples were aseptically transferred from the incubation plate to a fresh 24-well plate and immersed in 1 ml of *Bac*Light LIVE/DEAD (Invitrogen, MA, USA) solution, containing equal proportions of propidium iodide and Syto9 at a concentration of 1.5 µl ml^{-1} of PBS. The plate was then incubated in the dark at room temperature for 15 min and imaged with an Olympus FV3000 confocal scanning laser microscope (CLSM; Olympus, Tokyo, Japan). Six random areas per disc were captured at 40x magnification. Fluorescence images were imported into ImageJ for quantification of the number of yeast cells and hyphal cells, and the lengths of hyphae. The percentage of hyphal cells on HTE-Ti and AR-Ti samples was calculated by $\frac{\text{Total hyphal cells}}{\text{Total cells}} \times 100$.[55a] Hyphal length was measured from the yeast-hyphal junction to the apex of the hyphal filament.[59] A hyphal network was defined as all hyphal cells in physical contact, and the hyphal network size was counted as the number of hyphae per hyphal network. Morphogenesis metrics on the HTE-Ti surface were normalized to those on the AR-Ti surface by calculating a percentage reduction.

Colony Enumeration: At timepoints of 1, 3, 7, and 10 days, samples were retrieved from the 24-well plate, gently rinsed in PBS, and transferred to sterile screwcap tubes containing 1 ml PBS. Cells were detached by sonication for 2 min followed by vortexing for 30 s. Serial ten-fold dilutions were performed and 10 µl aliquots from each dilution were dropped onto YPD agar plates, then incubated overnight at 37 °C.[60] Colonies were counted after 24 h incubation and were used to calculate CFU per disc.

RNA Extraction and Purification: Samples previously immersed in RNA Later were sonicated for 2 min followed by vortexing for 30 s in 5 ml tubes to remove adhered cells from AR-Ti and HTE-Ti samples. The cell suspension was then centrifuged for 5 min at 12 000g to pellet the cells. The supernatant was discarded, and the pellet resuspended in lysis buffer provided with the RiboPure RNA Purification Kit (Invitrogen, USA). The RNA extractions were carried out following the manufacturer's instructions, adapted to generate a final product of 50 µl. Quantification and purity of the extracted RNA were determined using a NanoDrop 2000c Spectrophotometer (ThermoFisher, MA, USA).

Quantitative PCR (qPCR): PCR master mixes were assembled for each primer set using the SuperScript III Platinum One-Step qRT-PCR Kit (Invitrogen, CA, USA) according to the manufacturer's instructions. Primers were added at a concentration of 10 µM. RNA template (10 ng) was added to each reaction tube in 1 µl aliquots. No-template controls (NTCs) received 1 µl of RNAse-free H_2O instead. RNA was reverse transcribed to cDNA and amplified in 1 step in a Rotor-Gene Q Thermocycler (version 2.1.0, QIAGEN, Hilden, Germany) with the following program: 3 minutes hold at 50 °C; 5 min hold at 95 °C; 40*x* cycles of 95 °C for 15 s and 60 °C for 30 s. Fluorescent signal was acquired at 60 °C. A melting curve was generated between 72 and 95 °C at 1 °C increments. Amplification specificity was verified by melting curve analysis. qPCR data of target genes were normalized to the RPP2B data, which was chosen as a reference gene due to its stable expression observed on both AR-Ti and HTE-Ti surfaces. The normalized data were used to calculate relative gene expression ($2^{-\Delta Ct}$) and the data were plotted as a % change relative to the baseline (AR-Ti surface without serum supplementation). A list of the primers used in this study can be found in the supplementary information (Table S1, Supporting Information).

Antifungal Drug Sensitivity: Amphotericin B (AmB: Sigma-Aldrich, St. Louis, MO, USA) was dissolved into a stock concentration of 1 mg ml^{-1} in DMSO. The minimum inhibitory concentration of AmB was determined following CLSI standard testing with the only adjustment being the media, which was Spider media supplemented with 20% FCS instead of Mueller-Hinton Broth. To determine the sensitivity of established cultures to AmB, AR-Ti and HTE-Ti discs were incubated with *C. albicans* for 3 days at 37 °C with daily broth replenishment. After 3 days, samples were gently rinsed in PBS and transferred to a fresh 24-well plate. Samples were immersed in 1ml of Spider media supplemented with 20% FCS and 20 µg ml^{-1} AmB. The media and AmB were replenished daily for 7 days. Samples were analyzed for cell viability at days 1, 3, 5, and 7. Samples were stained with LIVE/DEAD BacLight Bacterial Viability Kit, containing equal proportions of Syto9 and Propidium Iodide at 1.5 µl ml^{-1} PBS, followed by 15 min of incubation in the dark at room temperature. Samples were inverted onto a glass coverslip, then imaged with an Olympus FV3000 CLSM, and full thickness biomass images were taken at 3 random locations per sample. Micrographs were analyzed using Imaris 3D analysis software (Version 9.3.0, Bitplane, Zürich, CHE) implementing the "surface" function to obtain total biovolume and dead biovolume.

Statistical Analysis: All experiments were performed in biological triplicate. All data except PCR were analyzed in GraphPad Prism v8.3.0 using a Student's *T*-test. Statistical analysis of qPCR data was performed in GraphPad Prism using a One-Way ANOVA using Tukey's multiple comparisons test, comparing % change in $2^{-\Delta Ct}$ relative to baseline. Statistical significance was defined as $P < 0.05$.

Supporting Information

Supporting Information is available from the Wiley Online Library or from the author.

Acknowledgements

This study was co-funded by the Department of Industry, Science, Energy and Resources (Innovative Manufacturing CRC Ltd) Global Orthopaedic Technology Pty Ltd (IMCRC/GOT/130318). The authors acknowledge the funding and in-kind support from Corin Australia and the University of South Australia. The authors would also like to acknowledge the instruments and scientific and technical assistance of Microscopy Australia at the University of South Australia, Mawson Lakes Campus, a facility that is funded by the University, and State and Federal Governments. K.V thanks NHMRC for Fellowship GNT1194466.

Open access publishing facilitated by University of South Australia, as part of the Wiley - University of South Australia agreement via the Council of Australian University Librarians.

© 2022 The Authors. Advanced Materials Interfaces published by Wiley-VCH GmbH

21967350, 2022, 12, Downloaded from https://onlinelibrary.wiley.com/doi/10.1002/admi.202102353 by Eddie Koiki Mabo Library, Wiley Online Library on [01/03/2023]. See the Terms and Conditions (https://onlinelibrary.wiley.com/terms-and-conditions) on Wiley Online Library for rules of use; OA articles are governed by the applicable Creative Commons License

Conflict of Interest

The authors declare no conflict of interest.

Author Contributions

A.H., R.B., T.B., D.B., and K.V. designed the experiments. A.H, R.B, J.W, D.P, and P.Z performed the experiments and analyzed the data. K.V. supervised the study and revised the manuscript. All authors took part in drafting the manuscript.

Data Availability Statement

The data that support the findings of this study are available from the corresponding author upon reasonable request.

Keywords

antifungal drugs, hydrothermal etching, implants, mechano-bactericidal effect, morphogenesis

Received: December 3, 2021
Revised: January 12, 2022
Published online: February 4, 2022

[1] a) M. Geetha, A. K. Singh, R. Asokamani, A. K. Gogia, *Prog. Mater. Sci.* **2009**, *54*, 397; b) R. B. Osman, M. V. Swain, *Materials* **2015**, *8*, 932.
[2] a) J. Parvizi, T. Gehrke, *J. Arthroplasty* **2014**, *29*, 1331; b) J. Parvizi, T. Gehrke, A. F. Chen, *Bone Joint J.* **2013**, *95-B*, 1450; c) J. M. Schierholz, J. Beuth, *J. Hosp. Infect.* **2001**, *49*, 87.
[3] a) P. Stoodley, S. Kathju, F. Z. Hu, G. Erdos, J. E. Levenson, N. Mehta, B. Dice, S. Johnson, L. Hall-Stoodley, L. Nistico, N. Sotereanos, J. Sewecke, J. C. Post, G. D. Ehrlich, *Clin. Orthop. Relat. Res.* **2005**, https://doi.org/10.1097/01.blo.0000175129.83084.d531; b) M. A. Cataldo, N. Petrosillo, M. Cipriani, R. Cauda, E. Tacconelli, *J. Infect.* **2010**, *61*, 443.
[4] K. Kordbacheh Changi, J. Finkelstein, P. N. Papapanou, *Clin. Oral Implants Res.* **2019**, *30*, 306.
[5] a) G. Ramage, J. P. Martínez, J. L. López-Ribot, *FEMS Yeast Res.* **2006**, *6*, 979; b) C. Gökmenoglu, N. B. Kara, M. Beldüz, A. Kamburoğlu, I. Tosun, E. Sadik, C. Kara, *Niger. J. Clin. Pract.* **2018**, *21*, 33; c) R. Bürgers, S. Hahnel, T. E. Reichert, M. Rosentritt, M. Behr, T. Gerlach, G. Handel, M. Gosau, *Acta Biomater.* **2010**, *6*, 2307; d) L. Escolà-Vergé, D. Rodríguez-Pardo, P. S. Corona, C. Pigrau, *Antibiotics* **2021**,*10*, 429.
[6] E. Monroy-Pérez, R. M. Rodríguez-Bedolla, J. Garzón, F. Vaca-Paniagua, E. Arturo-Rojas Jiménez, G. L. Paniagua-Contreras, *Microb. Pathog.* **2020**, *148*, 104436.
[7] M. M. Harriott, M. C. Noverr, *Antimicrob. Agents Chemother.* **2010**, *54*, 3746.
[8] F. L. Mayer, D. Wilson, B. Hube, *Virulence* **2013**, *4*, 119.
[9] G. D. Brown, D. W. Denning, N. A. R. Gow, S. M. Levitz, M. G. Netea, T. C. White, *Sci. Transl. Med.* **2012**, *4*, 165rv13.
[10] L. Y. Ngo, S. Kasahara, D. K. Kumasaka, S. E. Knoblaugh, A. Jhingran, T. M. Hohl, *J. Infect. Dis.* **2014**, *209*, 109.
[11] M. Whiteway, C. Bachewich, *Annu. Rev. Microbiol.* **2007**, *61*, 529.
[12] a) P. E. Sudbery, *Nat. Rev. Microbiol.* **2011**, *9*, 737; b) C. J. Nobile, J. E. Nett, D. R. Andes, A. P. Mitchell, *Eukaryotic Cell* **2006**, *5*, 1604.
[13] a) A. Correia, U. Lermann, L. Teixeira, F. Cerca, S. Botelho, R. M. Gil da Costa, P. Sampaio, F. Gärtner, J. Morschhäuser, M. Vilanova, C. Pais, *Infect. Immun.* **2010**, *78*, 4839; b) M. Gulati, C. J. Nobile, *Microbes Infect.* **2016**, *18*, 310.
[14] J. Chandra, D. M. Kuhn, P. K. Mukherjee, L. L. Hoyer, T. McCormick, M. A. Ghannoum, *J. Bacteriol.* **2001**, *183*, 5385.
[15] G. Ramage, S. P. Saville, B. L. Wickes, J. L. López-Ribot, *Appl. Environ. Microbiol.* **2002**, *68*, 5459.
[16] T. Vila, J. A. Romo, C. G. Pierce, S. F. McHardy, S. P. Saville, J. L. Lopez-Ribot, *Virulence* **2017**, *8*, 150.
[17] a) C. M. Bhadra, V. K. Truong, V. T. Pham, M. Al Kobaisi, G. Seniutinas, J. Y. Wang, S. Juodkazis, R. J. Crawford, E. P. Ivanova, *Sci. Rep.* **2015**, *5*, 16817; b) T. L. Clainche, D. Linklater, S. Wong, P. Le, S. Juodkazis, X. L. Guevel, J. L. Coll, E. P. Ivanova, V. Martel-Frachet, *ACS Appl. Mater. Interfaces* **2020**, *12*, 48272; c) J. Hasan, R. J. Crawford, E. P. Ivanova, *Trends Biotechnol.* **2013**, *31*, 295; d) E. P. Ivanova, J. Hasan, H. K. Webb, G. Gervinskas, S. Juodkazis, V. K. Truong, A. H. Wu, R. N. Lamb, V. A. Baulin, G. S. Watson, J. A. Watson, D. E. Mainwaring, R. J. Crawford, *Nat. Commun.* **2013**, *4*, 2838.
[18] D. P. Linklater, V. A. Baulin, S. Juodkazis, R. J. Crawford, P. Stoodley, E. P. Ivanova, *Nat. Rev. Microbiol.* **2020**, *19*, 8.
[19] a) J. V. Wandiyanto, S. Cheeseman, V. K. Truong, M. A. Kobaisi, C. Bizet, S. Juodkazis, H. Thissen, R. J. Crawford, E. P. Ivanova, *J. Mater. Chem. B* **2019**, *7*, 4424; b) R. Bright, D. Fernandes, J. Wood, D. Palms, A. Burzava, N. Ninan, T. Brown, D. Barker, K. Vasilev, *Mater. Today Bio* **2022**, *13*, 100176; c) J. V. Wandiyanto, T. Tamanna, D. P. Linklater, V. K. Truong, M. Al Kobaisi, V. A. Baulin, S. Joudkazis, H. Thissen, R. J. Crawford, E. P. Ivanova, *J. Colloid Interface Sci.* **2020**, *560*, 572.
[20] A. Hayles, J. Hasan, R. Bright, D. Palms, T. Brown, D. Barker, K. Vasilev, *Materials Today Chemistry* **2021**, *22*, 100622.
[21] S. B. Girois, F. Chapuis, E. Decullier, B. G. P. Revol, *Eur. J. Clin. Microbiol. Infect. Dis.* **2006**, *25*, 138.
[22] L. E. Cowen, *Nat. Rev. Microbiol.* **2008**, *6*, 187.
[23] V. Boddapati, M. C. Fu, D. J. Mayman, E. P. Su, P. K. Sculco, A. S. McLawhorn, *J. Arthroplasty* **2018**, *33*, 521.
[24] R. Bright, A. Hayles, D. Fernandes, R. M. Visalakshan, N. Ninan, D. Palms, A. Burzava, D. Barker, T. Brown, K. Vasilev, *ACS Appl. Mater. Interfaces* **2021**, *13*, 38007.
[25] a) B. D. Boyan, E. M. Lotz, Z. Schwartz, *Tissue Eng., Part A* **2017**, *23*, 1479; b) L. Lv, Y. Xie, K. Li, T. Hu, X. Lu, Y. Cao, X. Zheng, *Adv. Healthcare Mater.* **2018**, *7*, e1800675; c) S. M. Hamlet, R. S. B. Lee, H. J. Moon, M. A. Alfarsi, S. Ivanovski, *Clin. Oral Implants Res.* **2019**, *30*, 1085.
[26] C. H. Kowalski, K. A. Morelli, D. Schultz, C. D. Nadell, R. A. Cramer, *Proc. Natl. Acad. Sci. U S A* **2020**, *117*, 22473.
[27] a) A. Brand, *Int. J. Microbiol.* **2012**, *2012*, 517529; b) F. Mech, D. Wilson, T. Lehnert, B. Hube, M. Thilo Figge, *Cytometry, Part A* **2014**, *85*, 126.
[28] L. Popolo, T. Gualtieri, E. Ragni, *Med. Mycol.* **2001**, *39*, Suppl 1, 111.
[29] C. J. Heilmann, A. G. Sorgo, S. Mohammadi, G. J. Sosinska, C. G. de Koster, S. Brul, L. J. de Koning, F. M. Klis, *Eukaryotic Cell* **2013**, *12*, 254.
[30] J. R. Blankenship, S. Fanning, J. J. Hamaker, A. P. Mitchell, *PLoS Pathog.* **2010**, *6*, e1000752.
[31] A. J. Warenda, J. B. Konopka, *Mol. Biol. Cell* **2002**, *13*, 2732.
[32] J. Samot, M. Rouabhia, *Probiotics Antimicrob. Proteins* **2021**, *13*, 287.
[33] a) C. J. Nobile, D. R. Andes, J. E. Nett, F. J. Smith, F. Yue, Q. T. Phan, J. E. Edwards, S. G. Filler, A. P. Mitchell, *PLoS Pathog.* **2006**, *2*, e63; b) C. J. Nobile, H. A. Schneider, J. E. Nett, D. C. Sheppard, S. G. Filler, D. R. Andes, A. P. Mitchell, *Curr. Biol.* **2008**, *18*, 1017.
[34] a) Y. Liu, S. G. Filler, *Eukaryotic Cell* **2011**, *10*, 168; b) C. J. Nobile, A. P. Mitchell, *Curr. Biol.* **2005**, *15*, 1150.
[35] a) R. Alves, C. Barata-Antunes, M. Casal, A. J. P. Brown, P. Van Dijck, S. Paiva, *PLoS Pathog.* **2020**, *16*, e1008478; b) A. Felk, M. Kretschmar,

© 2022 The Authors. Advanced Materials Interfaces published by Wiley-VCH GmbH

21967350, 2022, 12, Downloaded from https://onlinelibrary.wiley.com/doi/10.1002/admi.202102353 by Eddie Koiki Mabo Library, Wiley Online Library on [01/03/2023]. See the Terms and Conditions (https://onlinelibrary.wiley.com/terms-and-conditions) on Wiley Online Library for rules of use; OA articles are governed by the applicable Creative Commons License

A. Albrecht, M. Schaller, S. Beinhauer, T. Nichterlein, D. Sanglard, H. C. Korting, W. Schäfer, B. Hube, *Infect. Immun.* **2002**, *70*, 3689.
[36] a) C. J. Barelle, V. M. Duncan, A. J. Brown, N. A. Gow, F. C. Odds, *J. Antimicrob. Chemother.* **2008**, *61*, 315; b) C. do Rosário Esteves Guimarães, H. F. de Freitas, T. F. Barros, *Mol. Biol. Rep.* **2019**, *46*, 6147.
[37] J. M. Slauch, *Mol. Microbiol.* **2011**, *80*, 580.
[38] J. Jenkins, J. Mantell, C. Neal, A. Gholinia, P. Verkade, A. H. Nobbs, B. Su, *Nat. Commun.* **2020**, *11*, 1626.
[39] M. I. Ishak, X. Liu, J. Jenkins, A. H. Nobbs, B. Su, *Coatings* **2020**, 10.
[40] P. H. J. van der Voort, E. C. Boerma, J. P. Yska, *J. Antimicrob. Chemother.* **2007**, *59*, 952.
[41] E. Grela, A. Zdybicka-Barabas, B. Pawlikowska-Pawlega, M. Cytrynska, M. Wlodarczyk, W. Grudzinski, R. Luchowski, W. I. Gruszecki, *Sci. Rep.* **2019**, *9*, 17029.
[42] S. Costa-de-Oliveira, A. G. Rodrigues, *Microorganisms* **2020**, *8*, 154.
[43] a) M. A. Jabra-Rizk, W. A. Falkler, T. F. Meiller, *Emerging Infect. Dis.* **2004**, *10*, 14; b) J. Yan, B. L. Bassler, *Cell Host Microbe* **2019**, *26*, 15; c) D. Sharma, L. Misba, A. U. Khan, *Antimicrob. Resist. Infect. Control* **2019**, *8*, 76; d) C. W. Hall, T. F. Mah, *FEMS Microbiol. Rev.* **2017**, *41*, 276.
[44] T. Watamoto, L. P. Samaranayake, J. A. Jayatilake, H. Egusa, H. Yatani, C. J. Seneviratne, *Int. J. Antimicrob. Agents* **2009**, *34*, 333.
[45] D. J. Laprade, M. S. Brown, M. L. McCarthy, J. J. Ritch, N. Austriaco, *Microb. Cell* **2016**, *3*, 285.
[46] a) A. Velic, J. Hasan, Z. Li, P. K. D. V. Yarlagadda, *Biophys. J.* **2021**, *120*, 217; b) S. Pogodin, J. Hasan, V. A. Baulin, H. K. Webb, V. K. Truong, T. H. Phong Nguyen, V. Boshkovikj, C. J. Fluke, G. S. Watson, J. A. Watson, R. J. Crawford, E. P. Ivanova, *Biophys. J.* **2013**, *104*, 835.
[47] F. M. Klis, P. de Groot, K. Hellingwerf, *Med. Mycol.* **2001**, *39*, Suppl 1:1–8.
[48] a) A. Cavallaro, S. Taheri, K. Vasilev, *Biointerphases* **2014**, *9*, 029005; b) K. Vasilev, J. Cook, H. J. Griesser, *Expert Rev. Med. Devices* **2009**, *6*, 553; c) K. Vasilev, S. S. Griesser, H. J. Griesser, *Plasma Processes Polym.* **2011**, *8*, 1010.
[49] a) V. B. Damodaran, N. S. Murthy, *Biomater. Res.* **2016**, *20*, 18; b) K. Vasilev, N. Poulter, P. Martinek, H. J. Griesser, *ACS Appl. Mater. Interfaces* **2011**, *3*, 4831; c) S. Taheri, A. Cavallaro, S. N. Christo, P. Majewski, M. Barton, J. D. Hayball, K. Vasilev, *ACS Biomater. Sci. Eng.* **2015**, *1*, 1278; d) A. Bidossi, M. Bottagisio, N. Logoluso, E. De Vecchi, *Int. J. Mol. Sci.* **2020**, 21; e) M. Zilberman, A. Kraitzer, O. Grinberg, J. J. Elsner, *Handb. Exp. Pharmacol.* **2010**, *197*, 115.
[50] a) J. Hasan, S. Jain, K. Chatterjee, *Sci. Rep.* **2017**, *7*, 41118; b) P. M. Tsimbouri, L. Fisher, N. Holloway, T. Sjostrom, A. H. Nobbs, R. M. Meek, B. Su, M. J. Dalby, *Sci. Rep.* **2016**, *6*, 36857.
[51] E. P. Ivanova, J. Hasan, H. K. Webb, V. K. Truong, G. S. Watson, J. A. Watson, V. A. Baulin, S. Pogodin, J. Y. Wang, M. J. Tobin, C. Löbbe, R. J. Crawford, *Small* **2012**, *8*, 2489.
[52] a) J. Meyer, G. Piller, C. A. Spiegel, S. Hetzel, M. Squire, *J. Bone Jt. Surg., Am. Vol.* **2011**, *93*, 2049; b) V. J. Suhardi, D. A. Bichara, S. Kwok, A. A. Freiberg, H. Rubash, H. Malchau, S. H. Yun, O. K. Muratoglu, E. Oral, *Nat. Biomed. Eng.* **2017**, *1*, 0080.
[53] K. Nowlin, A. Boseman, A. Covell, D. LaJeunesse, *J. R. Soc., Interface* **2015**, *12*, 20140999.
[54] a) S. Silva, C. F. Rodrigues, D. Araújo, M. E. Rodrigues, M. Henriques, *J Fungi (Basel)* **2017**, *3*, 8; b) G. Vediyappan, T. Rossignol, C. d'Enfert, *Antimicrob. Agents Chemother.* **2010**, *54*, 2096.
[55] a) L. Meng, H. Zhao, S. Zhao, X. Sun, M. Zhang, Y. Deng, *Antimicrob. Agents Chemother.* **2019**, *63*, e01891; b) F. Haque, M. Alfatah, K. Ganesan, M. S. Bhattacharyya, *Sci. Rep.* **2016**, *6*, 23575; c) M. S. Ahmad Khan, F. Alshehrei, S. B. Al-Ghamdi, M. A. Bamaga, A. S. Al-Thubiani, M. Z. Alam, *Future Sci. OA* **2020**, *6*, FSO440.
[56] N. V. Kollu, D. R. LaJeunesse, *ACS Omega* **2021**, *6*, 1361.
[57] E. P. Ivanova, D. P. Linklater, A. A. Medina, P. Le, V. A. Baulin, H. Khuong Duy Nguyen, R. Curtain, E. Hanssen, G. Gervinskas, S. Hock Ng, V. Khanh Truong, P. Luque, G. Ramm, H. A. B. Wösten, R. J. Crawford, S. Juodkazis, S. Maclaughlin, *J. Colloid Interface Sci.* **2021**, DOI: https://doi.org/10.1016/j.jcis.2021.06.093.
[58] L. J. Douglas, *Trends Microbiol.* **2003**, *11*, 30.
[59] J. Westman, G. Moran, S. Mogavero, B. Hube, S. Grinstein, *mBio* **2018**, 9.
[60] S. Sieuwerts, F. A. M. De Bok, E. Mols, W. M. De Vos, J. E. T. Van Hylckama Vlieg, *Lett. Appl. Microbiol.* **2008**, *47*, 275.

© 2022 The Authors. Advanced Materials Interfaces published by Wiley-VCH GmbH

21967350, 2022, 12, Downloaded from https://onlinelibrary.wiley.com/doi/10.1002/admi.202102353 by Eddie Koiki Mabo Library, Wiley Online Library on [01/03/2023]. See the Terms and Conditions (https://onlinelibrary.wiley.com/terms-and-conditions) on Wiley Online Library for rules of use; OA articles are governed by the applicable Creative Commons License